

High-resolution radio imaging of TGSS J1530+1049, a radio galaxy in a dense environment at $z = 4$

K. É. Gabányi^{1, 2, 3, 4, 5}, S. Frey^{2, 4, 6}, L. I. Gurvits^{7, 8}, Z. Paragi⁷, K. Perger^{2, 4}, A. Saxena^{9, 10}, R. A. Overzier^{11, 12, 13}, M. Villar-Martín¹⁴, V. Reynaldi^{15, 16}, G. Miley¹¹, H. J. A. Röttgering¹¹, A. Humphrey^{17, 18}, and Gy. Mező^{2, 4}

¹ Department of Astronomy, Institute of Physics and Astronomy, ELTE Eötvös Loránd University, Pázmány Péter sétány 1/A, 1117 Budapest, Hungary
e-mail: k.gabanyi@astro.elte.hu

² Konkoly Observatory, HUN-REN Research Centre for Astronomy and Earth Sciences, Konkoly-Thege Miklós út 15-17, 1121 Budapest, Hungary

³ HUN-REN-ELTE Extragalactic Astrophysics Research Group, ELTE Eötvös Loránd University, Pázmány Péter sétány 1/A, 1117 Budapest, Hungary

⁴ CSFK, MTA Centre of Excellence, Konkoly-Thege Miklós út 15-17, 1121 Budapest, Hungary

⁵ Institute of Astronomy, Faculty of Physics, Astronomy and Informatics, Nicolaus Copernicus University, Grudziądzka 5, 87-100 Toruń, Poland

⁶ Institute of Physics and Astronomy, ELTE Eötvös Loránd University, Pázmány Péter sétány 1/A, 1117 Budapest, Hungary

⁷ Joint Institute for VLBI ERIC, Oude Hoogeveensedijk 4, 7991 PD Dwingeloo, The Netherlands

⁸ Faculty of Aerospace Engineering, Delft University of Technology, Kluyverweg 1, 2629 HS, Delft, The Netherlands

⁹ Department of Physics, University of Oxford, Denys Wilkinson Building, Keble Road, Oxford, OX1 3RH, UK

¹⁰ Department of Physics and Astronomy, University College London, Gower Street, London WC1E 6BT, UK

¹¹ Leiden Observatory, University of Leiden, Niels Bohrweg 2, 2333 CA Leiden, The Netherlands

¹² Observatório Nacional/MCTI, Rua General José Cristino, 77, São Cristóvão, Rio de Janeiro, RJ 20921 400, Brazil

¹³ TNO, Oude Waalsdorperweg 63, 2597 AK Den Haag, The Netherlands

¹⁴ Centro de Astrobiología (CAB), CSIC-INTA, Ctra. de Ajalvir, km 4, E-28850 Torrejón de Ardoz, Madrid, Spain

¹⁵ Instituto de Astrofísica de La Plata, CONICET – UNLP, Paseo del Bosque, B1900FWA La Plata, Argentina

¹⁶ Facultad de Ciencias Astronómicas y Geofísicas, Universidad Nacional de La Plata, B1900FWA La Plata, Argentina

¹⁷ DTx – Digital Transformation CoLab, Building 1, Azurém Campus, University of Minho, 4800-058 Guimarães, Portugal

¹⁸ Faculdade de Ciências da Universidade do Porto, Rua do Campo de Alegre, 4150-007, Porto, Portugal

Received xx, 2025; accepted

ABSTRACT

Context. High-redshift radio galaxies can provide important insights into the structure formation and galaxy evolution at earlier cosmological epochs. TGSS J1530+1049 was selected as a candidate high-redshift radio galaxy, based on its very steep radio spectrum. Subsequent observations with the *James Webb Space Telescope* (*JWST*) presented in a companion paper (Saxena et al., submitted) have shown that it is located at a redshift $z = 4.0$. The *JWST* data furthermore showed that the radio source is part of one of the densest structures of galaxies and ionized gas known at these redshifts. The complex system qualitatively resembles a massive (cluster) galaxy forming early through a rapid succession of mergers.

Aims. TGSS J1530+1049 is an unresolved source down to $\sim 0.6''$ scale in multiple radio surveys. To reveal its high-resolution radio structure and allow for a detailed comparison with *JWST* observations, we studied its morphology at various angular scales with different radio interferometric instruments.

Methods. We observed TGSS J1530+1049 at milliarcsecond (mas) scale angular resolution with the European VLBI Network (EVN), and at ~ 100 -mas scale resolution with the enhanced Multi-Element Remotely Linked Interferometer Network (e-MERLIN).

Results. We recovered a complex north–south oriented structure with steep-spectrum radio-emitting features, which are associated with lobes and hot spots of a jetted active galactic nucleus. However, the centre of the radio galaxy proved to be too faint at cm wavelengths to be unambiguously detected in our observations. Nevertheless, the linear size (~ 5.5 kpc) and the radio power ($L_{1.4\text{GHz}} \approx 3 \times 10^{27} \text{ W Hz}^{-1}$) place it among the so-called medium-sized symmetric objects, a smaller and/or confined version of larger radio galaxies. Comparison between the radio morphology and that of the ionized gas as observed with the NIRSpec IFU on *JWST* shows that the two are closely aligned. However, the optical emission line gas extends out to ~ 25 kpc, which is well beyond the detected radio structures.

Key words. galaxies: active – galaxies: jets – galaxies: high-redshift – galaxies: individual: TGSS J1530+1049 – radio continuum: galaxies – techniques: interferometric

1. Introduction

High-redshift ($z \gtrsim 4$) active galactic nuclei (AGN) are essential in studying the growth of supermassive black holes (SMBH) and

the galaxy evolution in the early Universe. The radio-emitting subsample of these sources is of great importance since they can be studied with the highest angular resolution provided by radio interferometric technique. Among them, high-redshift radio galaxies are important constituents to study the evolution of large-scale structure in the Universe since they are often found in the centre of clusters and proto-clusters, and can be the progenitors of massive galaxies. At early cosmological epochs, the radio galaxies are expected to be young, compact systems.

Historically, it was proposed that compact radio sources with ultra-steep radio spectra could be good candidates for high-redshift radio galaxies (e.g., Blumenthal & Miley 1979; Roettgering et al. 1994; Chambers et al. 1996). Various authors use different definitions for the ultra-steep-spectrum (USS) sources (see, e.g., Braude et al. (1995), and, for a later summary, Coppejans et al. (2017)), but more recently Saxena et al. (2018a) collected a sample of USS sources with radio spectral indices $\alpha < -1.3$ (α is defined as $S \propto \nu^\alpha$, where S is the flux density and ν the observing frequency) measured between 150 MHz and 1.4 GHz. To enable further efficient selection of potential high-redshift sources, Saxena et al. (2018a) focused on those which remained undetected in optical and infrared surveys.

TGSS J1530+1049 (hereafter J1530+1049) was one of the brightest objects in their sample. In a follow-up radio observation of the sample, conducted with the Karl G. Jansky Very Large Array (VLA) at 1.4 GHz in its most extended A configuration, J1530+1049 was detected as a source well-described by a single Gaussian brightness distribution with a deconvolved size of $\sim 0.6''$, and a flux density of (7.5 ± 0.1) mJy. Optical spectroscopic observation at the radio position revealed a single emission line that was erroneously identified as a Lyman- α line at $z = 5.72$ (Saxena et al. 2018b). However, recent *James Webb Space Telescope* (JWST) imaging and spectroscopic observations of the object presented in a companion paper (Saxena et al. submitted) have revealed that the radio emission positionally coincides with a highly complex system consisting of several massive galaxies, diffuse emission and ionized gas knots at $z = 4.0$. The picture that has emerged is that of a dense core of interacting galaxies including the host galaxy of the radio source, perhaps signaling the formation of a very massive (central cluster) galaxy.

We observed J1530+1049 with the technique of very long baseline interferometry (VLBI) using the European VLBI Network (EVN) and the enhanced Multi-Element Remotely Linked Interferometer Network (e-MERLIN) to resolve its radio emission. Preliminary results of the EVN observation were presented in Gabányi et al. (2018), which used the redshift estimate available at that time. In Sect. 2, we describe the observations and data reduction. Results are presented in Sect. 3, while our findings are discussed in Sect. 4. The paper is concluded by a summary in Sect. 5.

In the following, we assume a Λ Cold Dark Matter cosmological model with a Hubble constant of $H_0 = 67.7 \text{ km s}^{-1} \text{ Mpc}^{-1}$, matter density parameter of $\Omega_m = 0.31$, and dark energy density parameter of $\Omega_\Lambda = 0.69$. At $z = 4.0$, the angular size of 1 milliarcsecond (mas) corresponds to 7.1 pc linear size, and the luminosity distance of the source is $D_L = 36676.4 \text{ Mpc}$ (Wright 2006).

2. Observations and data reduction

2.1. EVN observation

The EVN observation of J1530+1049 was conducted on 2018 September 19 at 1.7 GHz frequency (project code: RSG11) in e-VLBI mode (Szomoru 2008). The observing bandwidth was divided into 8 intermediate frequency channels (IF) with 16 MHz bandwidth each. The following antennas provided data: a single antenna of the Westerbork Synthesis Radio Telescope (the Netherlands), Effelsberg (Germany), Medicina (Italy), Onsala (Sweden), Tianma (China), Toruń (Poland), Hartebeesthoek (South Africa), and Sardinia (Italy). Sardinia observed in only four IFs.

The observation was conducted in phase-referencing mode (Beasley & Conway 1995). The phase-reference calibrator, ICRF J152502.9+110744 (hereafter J1525+1107), and the target source were observed alternately, in cycles with 1.5 min time spent on the calibrator and 4.5 min on the target source. The total on-target integration time was 57.6 min.

The data were reduced with the National Radio Astronomy Observatory (NRAO) Astronomical Image Processing System (AIPS, Greisen 1990) following the standard procedure (e.g., Diamond 1995). A priori amplitude calibration was performed using system temperature measurements at the antenna sites. Ionospheric corrections were conducted based on the total electron content maps from global navigation satellite systems data, and parallactic angle correction was also done. Then fringe fitting was performed on the data of the phase-reference calibrator.

The resulting calibrator source data were imaged in the Difmap software (Shepherd 1997) via the hybrid mapping method, which involves subsequent usage of the CLEAN algorithm (Högbom 1974) and phase self-calibration iterations. As a final step of imaging, we performed amplitude self-calibration and obtained overall gain correction factors for the antennas. These gain corrections were then applied to the data within AIPS. Additionally, the resulting image of the phase-reference calibrator was read back into AIPS to be used for improving the fringe fit. The fringe-fit solutions of the phase-reference calibrator were applied to the target source, which was then imaged in Difmap. Due to the weakness of the main target object, no self-calibration was attempted.

2.2. e-MERLIN observations

The e-MERLIN observations (project code: CY8205) took place on 2019 January 29 and February 22 at 5 GHz, and on 2019 March 7 and 8 at 1.5 GHz. At 1.5 GHz, 8 IFs were used, each with a bandwidth of 64 MHz and divided into 128 spectral channels. However, no signal was recorded in IF7. At 5 GHz, 4 IFs were used, each with a bandwidth of 128 MHz and divided into 128 channels. At both frequencies, the Jodrell Bank Mk2, Pickmere, Darnhall, Knockin, Defford, and Cambridge antennas participated in the observations. The Lovell Telescope at Jodrell Bank also joined at 5 GHz on the second observing day.

Beside the target source, the following calibrators were observed: 3C 84 as a pointing calibrator, 3C 286 as a flux density calibrator, OQ 208 as a bandpass calibrator. The phase calibrator was the same radio quasar used in the EVN observation, (J1525+1107). The on-target integration time was ~ 9 h and ~ 13.2 h at 1.5 and 5 GHz, respectively.

The raw visibility data were pre-processed and calibrated with the e-MERLIN pipeline¹ using the Common Astronomy

¹ version 0.9

Table 1. Parameters of the Gaussian components fitted to the 1.7-GHz EVN visibility data of J1530+1049.

ID	S (mJy)	θ (mas)	ΔRA (mas)	ΔDec (mas)
A	1.96 ± 0.30	10.2 ± 1.0	–	–
B	0.62 ± 0.17	4.0 ± 0.8	31.7 ± 0.6	-404.8 ± 0.6

Notes: Col. 1 – component identifier, Col. 2 – flux density, Col. 3 – angular size (FWHM), Col. 4 – relative right ascension, Col. 5 – relative declination

Software Applications (CASA, McMullin et al. 2007; CASA Team et al. 2022)². Imaging was also performed in CASA. We exported the channel-averaged dataset and additionally imaged it in *Difmap*. The resulting maps agree with each other. Due to the weakness of the source, no self-calibration was performed.

2.3. JWST observations

J1530+1049 was observed with the *JWST/NIRSpec* in IFU mode on 2023 July 14–15 (PIs: R.A. Overzier and A. Saxena, program GO 1964). The results of that program involving additional observations with the *Hubble Space Telescope* and *JWST/NIRCam* are discussed in detail in Saxena et al. (submitted). In this paper, we present a comparison between the high-resolution radio data and a map of the $\text{H}\alpha$ emission as measured with the *NIRSpec* IFU (see Sect. 4.2). For details on the observations and construction of the $\text{H}\alpha$ map, we refer the reader to the companion paper by Saxena et al (submitted).

3. Results

3.1. EVN observation

Two compact features (labeled as A and B) were detected with the EVN at 1.7 GHz with a projected separation of ~ 400 mas (Fig. 1), corresponding to ~ 2.8 kpc at the redshift of the source.

The coordinates of the brighter, northern feature (A) are right ascension $\alpha = 15^{\text{h}}30^{\text{m}}49\overset{\text{s}}{.}89029 \pm 0\overset{\text{s}}{.}00013$, and declination $\delta = 10^{\circ}49'31\overset{\text{s}}{.}1754 \pm 0\overset{\text{s}}{.}002$. When calculating the positional error, we took into account the uncertainty of the coordinates of the phase-reference calibrator source (0.11 mas in right ascension and 0.18 mas in declination direction³), and the error arising from the phase-referencing technique which depends on the target and calibrator source separation, in our case $1^{\circ}45$. Rijsma et al. (2017) estimate this error to be ~ 2 mas. Pradel et al. (2006) obtained a close value of 1.5 mas via simulated VLBI observations. We used the larger, more conservative value. It should also be noted that the coordinates of the phase-reference calibrator source were measured at 8.4 GHz, while the EVN observation was conducted at 1.7 GHz. Frequency-dependent core shift (Sokolovsky et al. 2011) could cause a difference between the International Celestial Reference Frame (ICRF, Charlot et al. 2020) position determined at 8.4 GHz and the 1.7-GHz position of the calibrator.

To describe the emission quantitatively, we fitted the visibilities with circular Gaussian brightness distribution model components. Since self-calibration cannot be performed, the obtained flux densities are expected to be lower than the real value due to coherence loss (Martí-Vidal et al. 2010). Previous works (e.g.

Mosoni et al. 2006; Gabányi et al. 2019) estimated the coherence loss to be $\sim 25\%$. The parameters of the two fitted components are given in Table 1, where the flux densities have been increased to account for the coherence loss. The errors were calculated according to the formulae given by Fomalont (1999). For the flux density errors, another 10% was added in quadrature to account for the absolute amplitude calibration inaccuracies.

The brightness temperature of the features can be calculated as (e.g., Veres et al. 2010)

$$T_B = 1.22 \cdot 10^{12} \frac{S}{\nu^2 \theta^2} (1+z) \text{ K}, \quad (1)$$

where S is the flux density of the components measured in Jy, ν the observing frequency in GHz, and θ the full width at half-maximum (FWHM) size in mas. The values obtained are $T_B^A = (4.0 \pm 0.8) \cdot 10^7$ K and $T_B^B = (8.2 \pm 3.2) \cdot 10^7$ K for components A and B, respectively. Both values well exceed the upper limit given for star-forming galaxies by Condon (1992), $\sim 10^5$ K, indicating AGN-related radio emission.

3.2. e-MERLIN observations

With e-MERLIN, two features (designated as N and S) could be detected at 1.5 GHz with a separation of ~ 780 mas, as shown in Fig. 2. At 5 GHz, the brighter northern feature (N) is clearly detected with e-MERLIN. At the approximate distance of feature S, at ~ 700 mas from N, and in the same position angle as seen in Fig. 2, we recover an emission spot at $\sim 5\sigma$ image noise level at 5 GHz (Fig. 3).

We used *Difmap* to fit the visibilities with circular Gaussian features to quantify the radio emission. Note that the brightness distribution models were fitted directly to the interferometric visibility data and not in the image plane, so the component sizes obtained can be considered as deconvolved sizes. In the 1.5-GHz band, we averaged the adjacent IFs by two together before fitting the visibilities, to minimize bandwidth smearing effects, but to increase the signal-to-noise ratio. Since IF7 did not record data, IF8 had to be fitted as it is. In the first three 128 MHz-wide chunks (i.e. IF pairs), both components, N and S could be fitted in the 1.5-GHz band. In the last one, where the bandwidth was only 64 MHz, the signal-to-noise ratio was not adequate to reliably fit component S. In the 5-GHz band, the components N and S could only be modeled if we used the whole bandwidth for the fit. The parameters of the brighter component N agreed within the errors if the first and second halves of the 5-GHz band were fitted separately.

The results of the model fitting are given in Table 2. The errors have been estimated using the formulae of Fomalont (1999), and additional 20% and 10% were added quadratically to the flux density errors to account for the amplitude calibration uncertainty of e-MERLIN at 1.5 GHz and 5 GHz, respectively (Baldi et al. 2021; Horesh et al. 2020).

Both components have steep radio spectra (Fig. 4). Their spectral indices are $\alpha_N = -2.1 \pm 0.1$ and $\alpha_S = -1.7 \pm 0.5$.

4. Discussion

4.1. Astrometric registration of the radio components

The EVN-detected compact feature A falls within the region of the e-MERLIN-detected brightest feature, N, at 5 GHz. However, there is a significant, ~ 110 mas offset in the north–south direction between the peak positions measured in the 5-GHz and 1.5-GHz e-MERLIN observations. The question arises whether

² version 5.4

³ According to the latest Radio Fundamental Catalog (Petrov & Kovalev 2025) rfc2025b maintained by L. Petrov at https://astrogeo.org/sol/rfc/rfc_2025b/

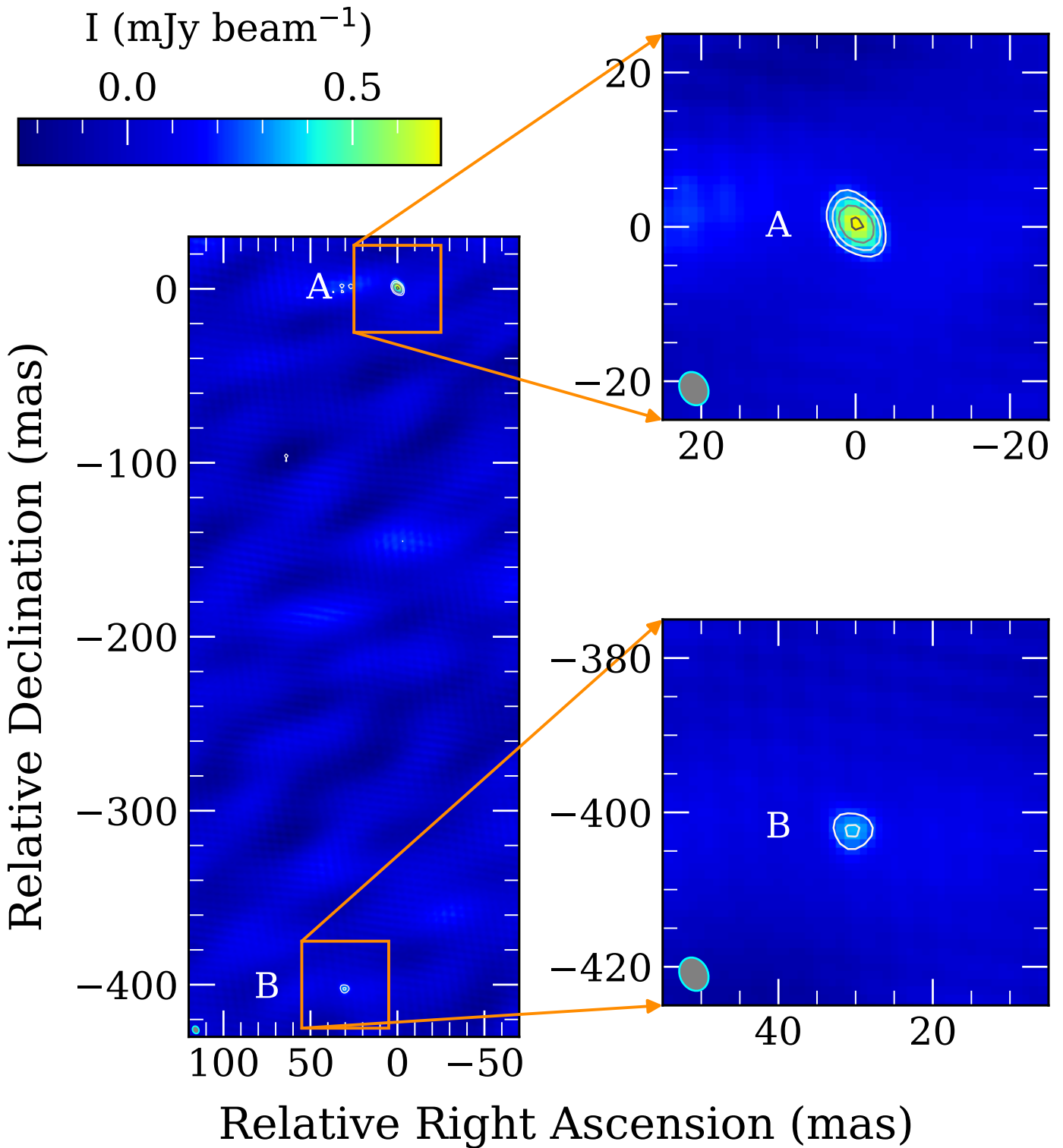


Fig. 1. EVN 1.7-GHz maps of J1530+1049. On the right-hand side, the two detected features are shown zoomed-in. The peak intensity of the whole image is $0.70 \text{ mJy beam}^{-1}$. The contour levels are at $(\pm 0.23, 0.33, 0.47, 0.66) \text{ mJy beam}^{-1}$. The lowest positive contour level corresponds to 5σ image noise. The restoring beam is shown in the lower left corner of the panels. Its FWHM size is $4.48 \text{ mas} \times 3.61 \text{ mas}$ at a position angle of 27° .

this offset is caused by some physical effect in the target source, J1530+1049, or due to a difference in the astrometric registrations of the 1.5- and 5-GHz e-MERLIN images.

The same phase-reference source (J1525+1107) was used in all observations. However, it has significant radio emission extended to ~ 100 -mas scale and the position of its brightness peak

can be different at different observing frequencies. To illustrate this, the e-MERLIN images of the calibrator are shown in Fig. 5, with a shift of ~ 110 mas between the image cutouts to facilitate their comparison. The north–south oriented double feature seen at 5 GHz cannot be resolved at 1.5 GHz with e-MERLIN. However, if the flux densities of the two components relative to

Table 2. Parameters of the Gaussian components fitted to the e-MERLIN visibility data of J1530+1049.

ν (GHz)	ID	S (mJy)	θ (mas)	ΔRA (mas)	ΔDec (mas)
1.318	N	5.7 ± 1.1	86.4 ± 2.3	–	–
	S	1.2 ± 0.3	116.0 ± 19.0	318 ± 21	-740 ± 47
1.446	N	3.7 ± 0.8	77.3 ± 8.7	–	–
	S	0.6 ± 0.2	31.7 ± 4.3	310 ± 19	-710 ± 42
1.574	N	2.3 ± 0.5	73.4 ± 3.2	–	–
	S	0.4 ± 0.1	63.5 ± 16.9	292 ± 17	-742 ± 39
1.734	N	3.2 ± 0.7	151.6 ± 8.1	–	–
5.072	N	0.25 ± 0.02	37.4 ± 3.1	–	–
	S	0.08 ± 0.03	76.5 ± 31.4	247 ± 6	-673 ± 14

Notes: Col. 1 – central frequency, Col. 2 – component identifier, Col. 3 – flux density, Col. 4 – angular size (FWHM), Col. 5 – relative right ascension, Col. 6 – relative declination

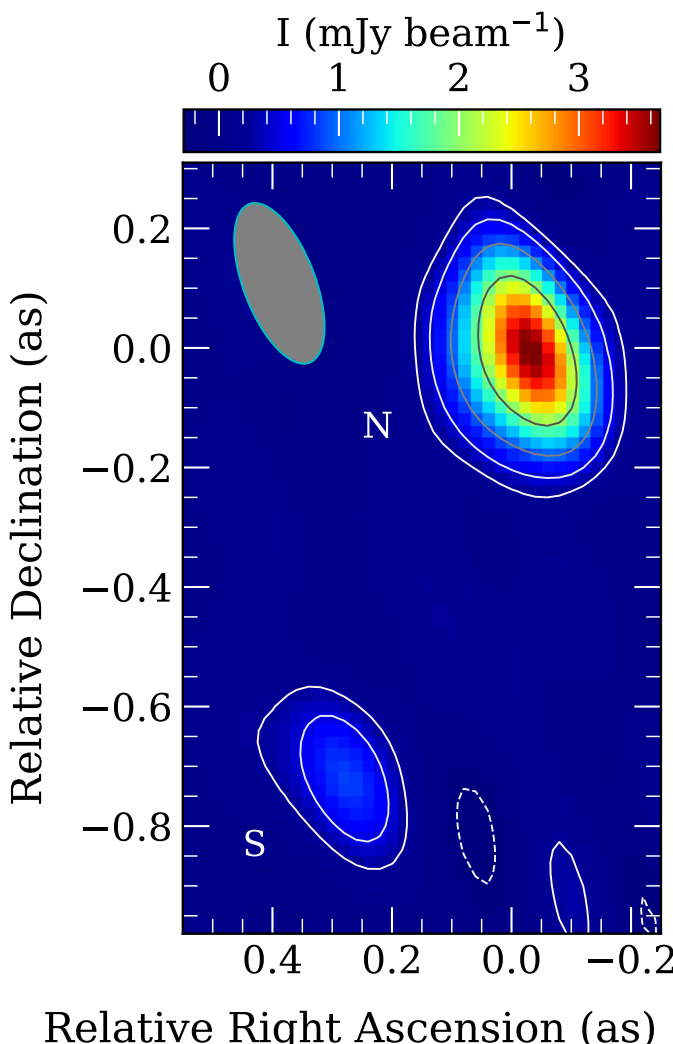


Fig. 2. 1.5-GHz e-MERLIN image of J1530+1049. The peak intensity is $3.7 \text{ mJy beam}^{-1}$. The lowest contours are drawn at $\pm 0.24 \text{ mJy beam}^{-1}$ corresponding to 6σ image noise level. Further positive contour levels increase by a factor of two. The restoring beam is shown in the upper left corner, its FWHM size is $284 \text{ mas} \times 120 \text{ mas}$ and its major axis is oriented at a position angle of 21° .

each other change with frequency, i.e. the northern feature has higher or very similar flux density than the southern one at the lower frequency of 1.5 GHz, then the position of the brightness

peak can shift towards the northern feature which, on the other hand, is relatively fainter at 5 GHz. This frequency-dependent change in the location of the brightness peak is further supported by higher-resolution VLBI images of the calibrator taken at 2.3 GHz, showing an extended bright feature to the north of the mas-scale compact emitting region (the core) at a distance of $\sim (120 - 150)$ mas. These archival images are available at the Astrogeo website⁴. Thus we can conclude that the positional mismatch between the 1.5-GHz and 5-GHz e-MERLIN images of J1530+1049 is caused by different brightness distributions of the phase-reference calibrator source at the two frequencies used (Fig. 5). Therefore, in our target source, the brighter northern features detected by e-MERLIN at the two frequencies (Figs. 2 and 3) are co-spatial, and the brighter EVN-detected component (A, Fig. 1) is located within this emitting region. Since the distances and position angles of the target morphology are very similar in the two e-MERLIN images, and no other significant radio emission can be detected in the field at either of the frequencies, we conclude that their cross-identification is solid.

4.2. The nature of the radio features

The fainter feature in the EVN image, component B (Fig. 1) cannot be seen in the e-MERLIN images, neither at 1.5 GHz (Fig. 2) nor at 5 GHz (Fig. 3). Its non-detection at 5 GHz could naturally be explained by the component having a steep spectrum, $\alpha \lesssim -2.4$, rendering it too faint for the sensitivity of the 5-GHz e-MERLIN observation. However, at the lower frequency, based on its brightness in the higher-resolution EVN image, it should have been visible at a similar significance level as component S. Nevertheless, the rms noise level of the image could have been estimated too optimistically. The 1σ rms noise level of the 1.5-GHz e-MERLIN image at the approximate position of component B is $\sim 0.13 \text{ mJy beam}^{-1}$, about 3 times larger than measured across the whole image, while the largest noise peak is $\sim 0.22 \text{ mJy beam}^{-1}$. Thus it could be that component B was just below the sensitivity limit of the 1.5-GHz e-MERLIN observation. Additionally, component B could also be variable. A flux density drop of $\sim 50\%$ within ~ 1.2 months time in the rest frame of the source (6 months elapsed between the EVN and e-MERLIN observations) is able to account for the non-detection of component B with the e-MERLIN at 1.5 GHz.

The high brightness temperatures of the EVN-detected features indicate AGN origin of the radio emission. While the EVN

⁴ http://astrogeo.org/cgi-bin/imdb_get_source.csh?source=J1525%2B1107 maintained by L. Petrov

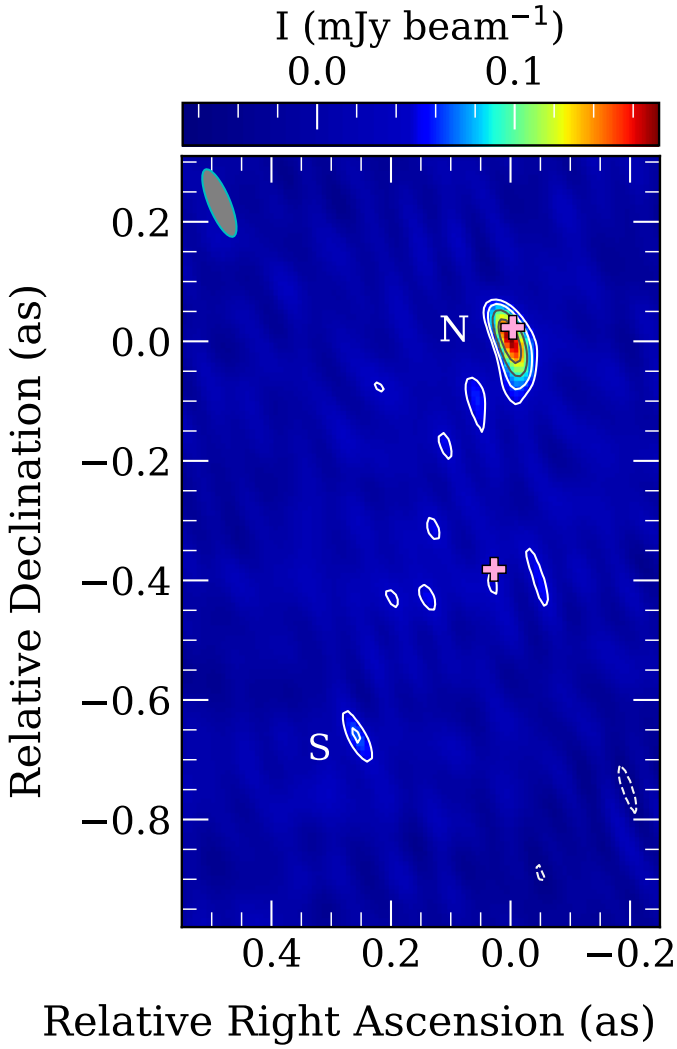


Fig. 3. 5-GHz e-MERLIN image of J1530+1049. The peak intensity is $0.17 \text{ mJy beam}^{-1}$. The lowest contours are drawn at $\pm 0.046 \text{ mJy beam}^{-1}$ corresponding to 3.5σ image noise level. Further positive contour levels increase by a factor of $\sqrt{2}$. The restoring beam is shown in the upper left corner, its FWHM size is $121 \text{ mas} \times 36 \text{ mas}$ and its major axis is oriented at a position angle of 23° . The pink crosses indicate the positions of the EVN-detected components.

observation was conducted at a single frequency only, one can use the dual-frequency e-MERLIN measurements to infer the power-law radio spectral index of component A (Fig. 4). If we assume that the 5-GHz flux density of component N is contained within a compact mas-scale feature, detectable with VLBI, it would imply a spectral index of $\alpha_A \approx -1.9$, thus steep radio spectrum. Such spectral index is often related to the lobe-like features seen in radio galaxies, while the cores of radio-loud AGN have usually flat or inverted radio spectra at cm wavelengths (e.g., Hovatta et al. 2014, and references therein).

At the position of feature S, there is no sign of any EVN detection, most probably indicating the resolved nature of this component. Moreover, feature S also has a steep radio spectrum indicated by the e-MERLIN data (Fig. 4). Due to the faintness of this feature at 5 GHz, also indicated by the large relative error of its spectral index, it may have even steeper radio spectrum than the one formally obtained, $\alpha_S \sim -1.7$. Thus, neither of the firmly detected radio features can be regarded as the central radio emitting region of the AGN that is expected to have flat or inverted

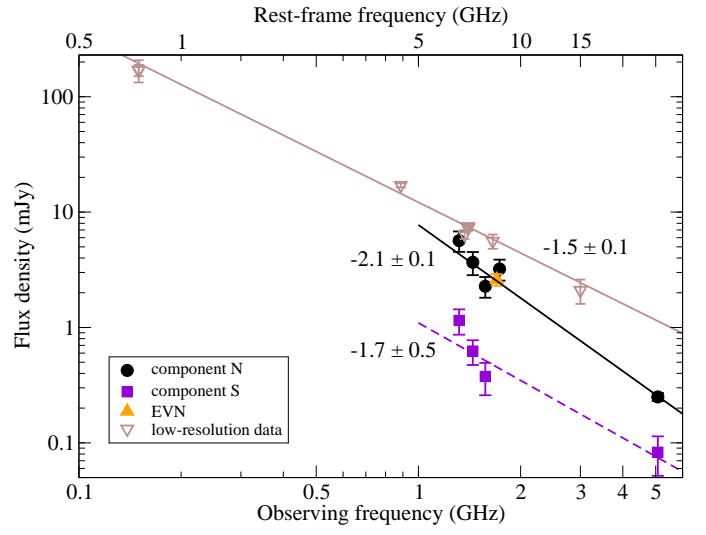


Fig. 4. The flux densities of the two Gaussian components that can be fitted to the e-MERLIN visibilities of J1530+1049. Circles and squares are for the components N and S, respectively. The solid and dashed lines are power-law fits to the corresponding data points. For comparison, the sum of the flux densities of the EVN-detected components is also shown with a yellow upward triangle. Empty downward brown triangles show lower-resolution flux density measurements from various surveys (see Sect. 4.3 for details), and the brown line indicates the power-law fit to those points. The numbers show the corresponding spectral indices.

synchrotron self-absorbed spectrum. The sizes and spectral indices of N and S are more compatible with extended jet-related emissions containing mas-scale compact hot spot such as feature A in the EVN observation.

The continuum-subtracted $\text{H}\alpha$ line emission, as obtained from the *JWST*/NIRSpec IFU observations, together with the results of the e-MERLIN radio observations are shown in Fig. 6. Several bright emission-line components lie along the general direction of the radio axis. The radio-emitting regions are close to two large ionized areas (labeled L1 and L3 in the paper by Saxena et al., submitted), but they do not coincide with either of them. Despite the absence of a radio core, based on the *JWST* observations, it is believed that the radio emission emerges from a bright optical continuum and emission-line source located in between the two radio hotspots (the object labeled C2 in Saxena et al. submitted). The *JWST* data furthermore shows evidence for perturbed gas, especially close to the location of the southern hotspot. Besides these jet–gas interactions, other sources likely contributing to the strong alignment observed are the ionization by a central, obscured active nucleus and an infalling low-mass starburst galaxy at the southern edge of the field (object C6 in Saxena et al., submitted).

4.3. Radio emission at larger scales

According to the 1.4-GHz NRAO VLA Sky Survey (Condon et al. 1998), J1530+1049 has a flux density of $(7.4 \pm 0.5) \text{ mJy}$. At the same frequency but with higher resolution, the Faint Images of the Radio Sky at Twenty-centimeters (FIRST) survey measured $(7.25 \pm 0.15) \text{ mJy}$ (Helfand et al. 2015). Saxena et al. (2018a) reported a similar flux density value, $(7.5 \pm 0.1) \text{ mJy}$, measured in a higher-resolution VLA A-configuration observation. More recently, J1530+1049 was detected in the the Rapid Australian Square Kilometre Array Pathfinder (ASKAP) Continuum Survey (RACS with flux densities of $(6.4 \pm 0.6) \text{ mJy}$, and

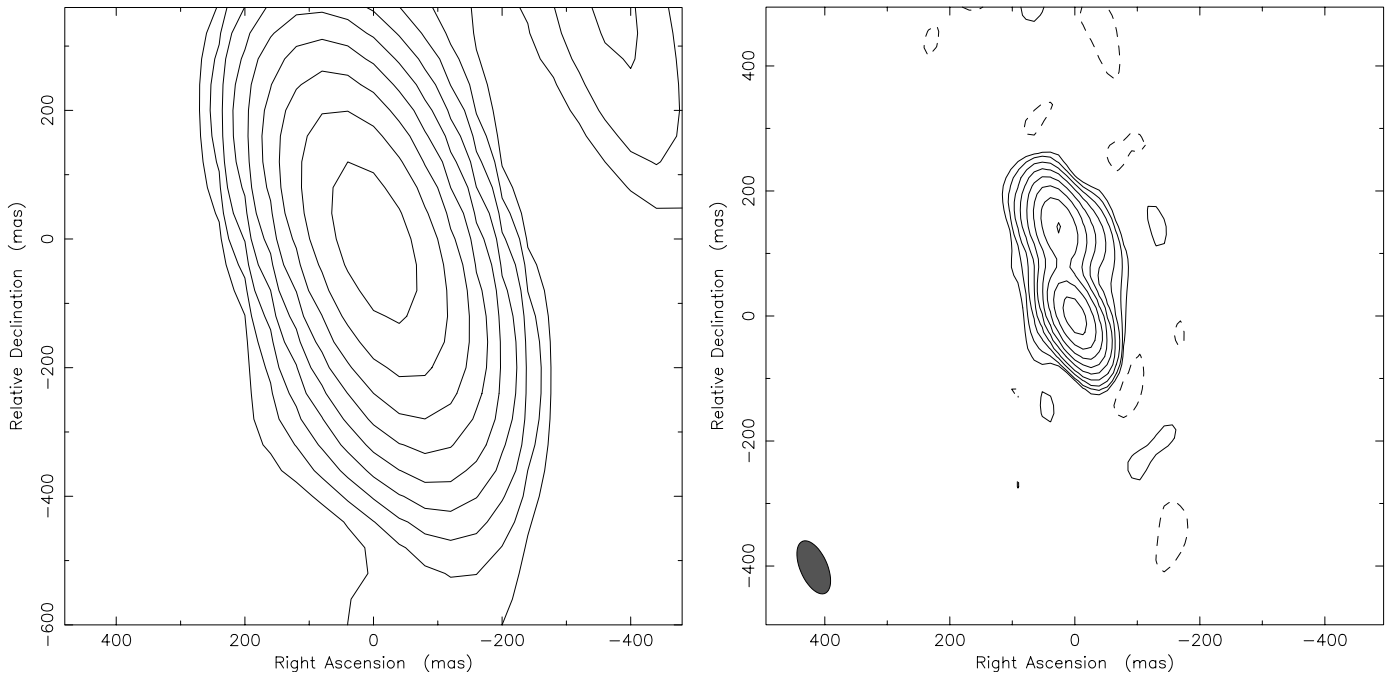


Fig. 5. The e-MERLIN images of the calibrator source, J1525+1107. *Left*: at 1.5-GHz. The peak intensity is $420 \text{ mJy beam}^{-1}$. The lowest positive contour is drawn at $1.1 \text{ mJy beam}^{-1}$ corresponding to 7σ image noise level. The FWHM size of the restoring beam is $321 \text{ mas} \times 144 \text{ mas}$ and its major axis is oriented at a position angle of 21° . *Right*: 5-GHz. The peak intensity is $274 \text{ mJy beam}^{-1}$. The lowest positive contour is drawn at $0.75 \text{ mJy beam}^{-1}$ corresponding to 7σ image noise level. The restoring beam is shown in the lower left corner, its FWHM size is $91 \text{ mas} \times 44 \text{ mas}$ and its major axis is oriented at a position angle of 24° . The two image cutouts have the same size. To illustrate that the 1.5-GHz peak corresponds to the secondary rather than the primary brightness peak at 5 GHz, the images are displaced by 110 mas with respect to each other in the declination direction.

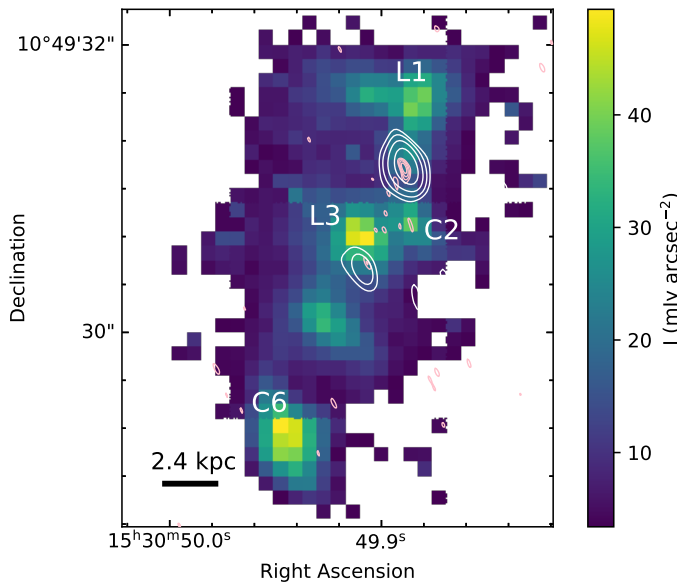


Fig. 6. Overlay of the *JWST* H α +[N II] emission line map from Saxena et al. (submitted) and the e-MERLIN maps of J1530+1049. The colour scale shows the continuum-subtracted H α line map, where low-significance pixels have been masked (for details, see Saxena et al., submitted). The white and pink contours represent the 1.5-GHz and the 5-GHz e-MERLIN data. Contour levels are the same as in Figs. 2, 3, except that negative contours are omitted for clarity. In the lower left corner the linear scale is displayed.

$(5.6 \pm 0.8) \text{ mJy}$ at 1.37 GHz, and 1.66 GHz , respectively (Duchesne et al. 2024, 2025). All these values exceed the sum of flux

densities of components N and S detected with e-MERLIN at close frequencies. However, no self-calibration was performed on the e-MERLIN data, therefore coherence loss can result in lower measured flux density values.

J1530+1049 was detected at 3 GHz in the three epochs of the VLA Sky Survey (VLASS, Lacy et al. 2020). We downloaded the three images from the Canadian Astronomy Data Centre (CADC⁵), and used AIPS to fit them with a single Gaussian. The flux densities agree within the error, their average value is $(2.1 \pm 0.5) \text{ mJy}$. This exceeds the flux density expected from the spectral indices derived from the e-MERLIN observations (Fig. 4), $\sim 1 \text{ mJy}$. While a frequency-independent coherence loss of the e-MERLIN data will not alter the obtained spectral index, it can underestimate the predicted 3-GHz flux density.

Below 1 GHz, J1530+1049 is brighter, as indicated by the lowest available frequency measurement of the RACS, 888 MHz (Hale et al. 2021), $(17.1 \pm 0.71) \text{ mJy}$, and by the TIFR Giant Meterwave Radio Telescope Sky Survey (TGSS, Intema et al. 2017) at 150 MHz, $(170 \pm 19) \text{ mJy}$ (Fig. 4). These low-resolution flux density values imply a spectral index of $\alpha_{0.15 \text{ GHz}}^{3 \text{ GHz}} = -1.5 \pm 0.1$, but also indicate a flattening of the radio spectrum between 888 MHz and 150 MHz, corresponding to $\sim 5 \text{ GHz}$ and 750 MHz , respectively, in the rest frame of the source at $z = 4$.

The 1.4-GHz radio power of J1530+1049 is between $\sim (3 - 4) \times 10^{27} \text{ W Hz}^{-1}$, depending on whether the highest 1.4-GHz flux density and the broad-band spectral index values are used, or whether the flux density and spectral index are taken from the e-MERLIN observations. The linear size of the source is $\sim 5.5 \text{ kpc}$. It is an order of magnitude fainter and smaller version

⁵ www.cadc-ccda.hia-iha.nrc-cnrc.gc.ca/en/vlass/, accessed on 12 Sep. 2025

of the radio galaxy J1420+1205 located at similar redshift ($z = 4.026$) and also showing several steep-spectrum features at 100-mas scale (Gabányi et al. 2021). The properties of J1530+1049 are similar to those of the high-power compact steep spectrum sources, or medium-sized symmetric objects as shown by e.g. An & Baan (2012).

5. Summary

We imaged the radio emission of a radio galaxy at $z = 4$, J1530+1049, both at mas-scale and 100-mas scale angular resolutions. We detected two faint, mas-scale compact features at ~ 2.8 kpc projected separation with the EVN at 1.7 GHz. Their high brightness temperature values clearly indicate AGN-related origin.

The northern one could be detected as part of a larger component in our e-MERLIN observation at 1.5 GHz and 5 GHz. At larger scales, we detected another steep-spectrum, extended component at ~ 5.5 kpc separation from the brightest feature in both e-MERLIN observations. According to the flux densities of the radio features, all have steep power-law spectra. Thus neither of them can be identified as the centre of the AGN. All these features are most probably related to the lobes or hot spots in the AGN, possibly also indicating places of interaction with the surrounding medium.

The radio power and linear extent of the object place it among the medium-sized symmetric objects which are smaller and presumably younger versions of radio galaxies. A comparison with recent observations with the *JWST* reveals that the compact radio source is embedded in a very dense region of merging galaxies. Bright knots of emission-line gas are strongly aligned with the radio axis, but are distributed over a total extent about five times larger than the size of the radio source. These data point to a picture of a massive, forming galaxy that hosts at least one active supermassive black hole interacting with the surrounding gas through its (compact) radio jets.

Acknowledgements. The European VLBI Network is a joint facility of independent European, African, Asian, and North American radio astronomy institutes. Scientific results from data presented in this publication are derived from the following EVN project code(s): RSG11. The e-VLBI research infrastructure in Europe was supported by the European Union's Seventh Framework Programme (FP7/2007-2013) under grant agreement number RI-261525 NEXPREs. The research leading to these results has received funding from the European Commission Horizon 2020 Research and Innovation Programme under grant agreement No. 730562 (RadioNet). e-MERLIN is a National Facility operated by the University of Manchester at Jodrell Bank Observatory on behalf of STFC. Scientific results from data presented in this publication are derived from the e-MERLIN project CY8205. On behalf of the "Interferometric studies of radio-loud active galactic nuclei" project, we are grateful for the possibility to use the HUN-REN Cloud (see Héder et al. 2022, <https://science-cloud.hu/>) which helped us achieve the results published in this paper. This project was supported by the HUN-REN Hungarian Research Network. KÉG and SF received funding from the Hungarian National Research, Development and Innovation Office (NKFIH) excellence grant TKP2021-NKTA-64). MVM research has been funded by grant Nr. PID2021-124665NB-I00 by the Spanish Ministry of Science and Innovation/State Agency of Research MCIN/AEI/10.13039/501100011033 and by "ERDF A way of making Europe".

Braude, S. Y., Sokolov, K. P., Sharykin, N. K., & Zakharenko, S. M. 1995, *Ap&SS*, 226, 245

CASA Team, Bean, B., Bhatnagar, S., et al. 2022, *PASP*, 134, 114501

Chambers, K. C., Miley, G. K., van Breugel, W. J. M., & Huang, J. S. 1996, *ApJS*, 106, 215

Charlot, P., Jacobs, C. S., Gordon, D., et al. 2020, *A&A*, 644, A159

Condon, J. J. 1992, *ARA&A*, 30, 575

Condon, J. J., Cotton, W. D., Greisen, E. W., et al. 1998, *AJ*, 115, 1693

Coppejans, R., van Velzen, S., Intema, H. T., et al. 2017, *MNRAS*, 467, 2039

Diamond, P. J. 1995, in *Astronomical Society of the Pacific Conference Series*, Vol. 82, *Very Long Baseline Interferometry and the VLBA*, ed. J. A. Zensus, P. J. Diamond, & P. J. Napier, 227

Duchesne, S., Ross, K., Thomson, A. J. M., et al. 2025, *PASA*, 42, 38

Duchesne, S. W., Grundy, J. A., Heald, G. H., et al. 2024, *PASA*, 41, e003

Fomalont, E. B. 1999, in *Astronomical Society of the Pacific Conference Series*, Vol. 180, *Synthesis Imaging in Radio Astronomy II*, ed. G. B. Taylor, C. L. Carilli, & R. A. Perley, 301

Gabányi, K. É., Frey, S., An, T., et al. 2021, *Astronomische Nachrichten*, 342, 1092

Gabányi, K. É., Frey, S., Gurvits, L. I., Paragi, Z., & Perger, K. 2018, *Research Notes of the American Astronomical Society*, 2, 200

Gabányi, K. É., Frey, S., Satyapal, S., Constantin, A., & Pfeifle, R. W. 2019, *A&A*, 630, L5

Greisen, E. W. 1990, in *Acquisition, Processing and Archiving of Astronomical Images*, 125–142

Hale, C. L., McConnell, D., Thomson, A. J. M., et al. 2021, *PASA*, 38, e058

Héder, M., Rigó, E., Medgyesi, D., et al. 2022, *Információ Társadalom*, 22, 128

Helfand, D. J., White, R. L., & Becker, R. H. 2015, *ApJ*, 801, 26

Högberg, J. A. 1974, *A&AS*, 15, 417

Horesh, A., Sfaradi, I., Ergon, M., et al. 2020, *ApJ*, 903, 132

Hovatta, T., Aller, M. F., Aller, H. D., et al. 2014, *AJ*, 147, 143

Intema, H. T., Jagannathan, P., Mooley, K. P., & Frail, D. A. 2017, *A&A*, 598, A78

Lacy, M., Baum, S. A., Chandler, C. J., et al. 2020, *PASP*, 132, 035001

Martí-Vidal, I., Ros, E., Pérez-Torres, M. A., et al. 2010, *A&A*, 515, A53

McMullin, J. P., Waters, B., Schiebel, D., Young, W., & Golap, K. 2007, in *Astronomical Society of the Pacific Conference Series*, Vol. 376, *Astronomical Data Analysis Software and Systems XVI*, ed. R. A. Shaw, F. Hill, & D. J. Bell, 127

Mosoni, L., Frey, S., Gurvits, L. I., et al. 2006, *A&A*, 445, 413

Petrov, L. Y. & Kovalev, Y. Y. 2025, *ApJS*, 276, 38

Pradel, N., Charlot, P., & Lestrade, J. F. 2006, *A&A*, 452, 1099

Rioja, M. J., Dodson, R., Orosz, G., Imai, H., & Frey, S. 2017, *AJ*, 153, 105

Roettgering, H. J. A., Lacy, M., Miley, G. K., Chambers, K. C., & Saunders, R. 1994, *A&AS*, 108, 79

Saxena, A., Jagannathan, P., Röttgering, H. J. A., et al. 2018a, *MNRAS*, 475, 5041

Saxena, A., Marinello, M., Overzier, R. A., et al. 2018b, *MNRAS*, 480, 2733

Shepherd, M. C. 1997, in *Astronomical Society of the Pacific Conference Series*, Vol. 125, *Astronomical Data Analysis Software and Systems VI*, ed. G. Hunt & H. Payne, 77

Sokolovsky, K. V., Kovalev, Y. Y., Pushkarev, A. B., & Lobanov, A. P. 2011, *A&A*, 532, A38

Szomoru, A. 2008, in *The role of VLBI in the Golden Age for Radio Astronomy*, Vol. 9, 40

Veres, P., Frey, S., Paragi, Z., & Gurvits, L. I. 2010, *A&A*, 521, A6

Wright, E. L. 2006, *PASP*, 118, 1711

References

An, T. & Baan, W. A. 2012, *ApJ*, 760, 77

Baldi, R. D., Williams, D. R. A., McHardy, I. M., et al. 2021, *MNRAS*, 500, 4749

Beasley, A. J. & Conway, J. E. 1995, in *Astronomical Society of the Pacific Conference Series*, Vol. 82, *Very Long Baseline Interferometry and the VLBA*, ed. J. A. Zensus, P. J. Diamond, & P. J. Napier, 327

Blumenthal, G. & Miley, G. 1979, *A&A*, 80, 13